Polar-drive designs for optimizing neutron yields on the National Ignition Facility

A. M. Cok,[a] R. S. Craxton, and P. W. McKenty
Laboratory for Laser Energetics, University of Rochester, 250 East River Road, Rochester, New York 14623, USA

(Received 8 February 2008; accepted 4 August 2008; published online 25 August 2008)

Polar-drive designs are proposed for producing symmetric implosions of thin-shell, DT gas-filled targets leading to high fusion-neutron yields for neutron-diagnostic development. The designs can be implemented as soon as the National Ignition Facility (NIF) [E. M. Campbell and W. J. Hogan, Plasma Phys. Control. Fusion **41**, B39 (1999)] is operational as they use indirect-drive phase plates. Two-dimensional simulations using the hydrodynamics code SAGE [R. S. Craxton and R. L. McCrory, J. Appl. Phys. **56**, 108 (1984)] have shown that good low-mode uniformity can be obtained by choosing combinations of pointing and defocusing of the beams, including pointing offsets of individual beams within some of the NIF laser-beam quads. The optimizations have been carried out for total laser energies ranging from 350 kJ to 1.5 MJ, enabling the optimum pointing and defocusing parameters to be determined through interpolation for any given laser energy in this range. Neutron yields in the range of 10^{15}–10^{16} are expected. © *2008 American Institute of Physics*. [DOI: 10.1063/1.2975213]

I. INTRODUCTION

Considerable interest has been devoted to polar drive (PD) (Refs. 1–5) as a means of obtaining uniform direct-drive implosions on the National Ignition Facility (NIF) (Ref. 6) using just the indirect-drive rings of beams. While the NIF target chamber was designed with additional ports at 77.45° and 102.55° from the vertical (z) axis to accommodate direct drive,[7,8] it is anticipated that the optics necessary to divert half of the NIF beams into these ports will not be available for several years. Polar drive involves repointing the NIF beams toward the equator to provide the most uniform drive possible. Phase plates with appropriately chosen spot sizes (comparable to the size of the target) and spot shapes (sometimes elliptical) are required.

One important PD application is optimizing the high-neutron-yield targets for early NIF experiments designed to test the neutron diagnostics that will be used for ignition experiments. A minimum of 10^{15} neutrons is required for this purpose.[9] Before the NIF cryogenic system is operational, high yields can best be obtained from room-temperature, thin-walled, DT-filled targets irradiated with laser pulses a few nanoseconds in length. Similar targets (with glass wall thicknesses ranging from 2 to 3 μm and plastic coatings up to 2 μm thick) were used[10] on the OMEGA laser system[11] to obtain the highest thermonuclear yield (10^{14} DT neutrons) and yield efficiency (1% of scientific break even) achieved to date in laser-fusion experiments. These targets disassemble rapidly as they implode and produce high ion temperatures but low fuel densities. They are not greatly sensitive to speckle nonuniformities in the laser beams, and indeed phase plates were not used for the experiments described in Ref. 10. Even though the beams were totally unsmoothed and used away from best focus the yields were ~40% of one-dimensional (1D) predictions.

The NIF designs considered here use thin shells of glass (SiO_2) and plastic (CH) driven by 192 laser beams smoothed using indirect-drive phase plates. It is necessary to use these phase plates as direct-drive phase plates will not initially be available. The phase plates will be used away from the best focus as they are designed to produce focal-spot sizes that are significantly smaller than the target diameters of the proposed designs. Additional enlargement and shaping of the focal spot is accomplished by imposing small pointing differences among the four beams of each NIF quad.[12]

The 1D designs were developed using the hydrodynamics code LILAC,[13] and the beam pointings and defocus distances were optimized using the two-dimensional (2D) hydrodynamics code SAGE.[14] The optimum parameters (three pointing parameters and one defocus parameter for each of the four rings of beams) were found for four laser energies ranging from 350 kJ to 1.5 MJ. These parameters were then fit as functions of energy, enabling the optimum pointing and defocus parameters to be readily obtained for any energy in this range. Simulations have demonstrated that the interpolated parameters result in comparably good uniformity.

The outline of this paper is as follows: Sec. II describes the pointing and focusing parameters available for optimizing the designs, shows some predicted focal spots, and presents results from OMEGA that indicate that the focal shape can probably be calculated with a high degree of accuracy. Section III describes an optimized design at 350 kJ. Section IV shows how interpolated designs can be obtained anywhere in the range of 350 kJ–1.5 MJ and gives the anticipated yields within this range. Section V presents the main conclusion: That targets designed for high neutron yields can be imploded uniformly on the NIF using indirect-drive hardware before the NIF is ready for ignition experiments.

[a]Also at Allendale Columbia High School, Rochester, New York.

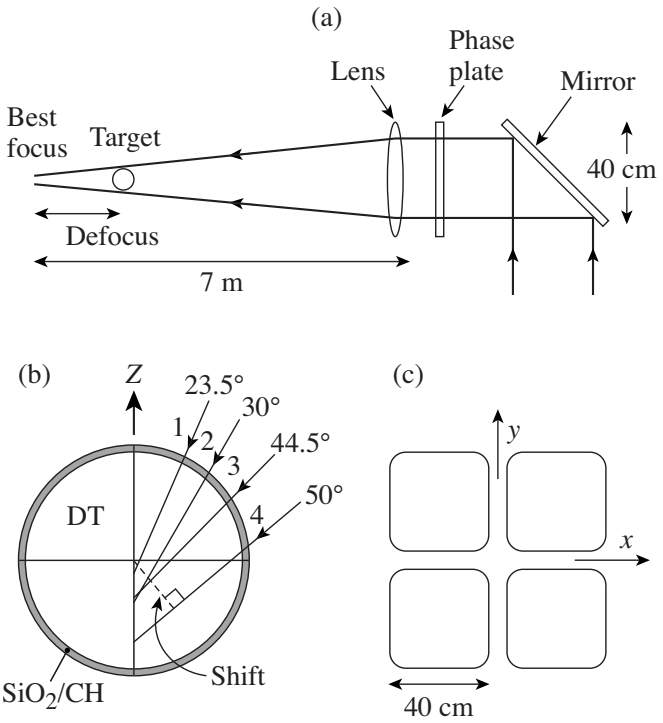

FIG. 1. (a) Schematic illustrating the components of the final NIF optical system relevant to the parameters varied in this work. The phase plate and defocus determine the beam shape on target and the mirror determines the (two) pointing shifts. (b) Beam-pointing shifts for the four NIF rings for a 350 kJ target. The shift of each beam is measured perpendicular to its propagation direction, as illustrated by the dashed line for ring 4. (c) Schematic of the arrangement of the four beams in a quad at the output of the laser. The overlapped on-target spatial profile produced by the quad can be adjusted by applying relative shifts to the beams in the x and y directions.

II. PARAMETERS AVAILABLE FOR OPTIMIZATION

The key parameters used to develop the 2D designs are specifications for pointing the beams away from the center of the target and defocusing the beams. The pointing shifts include "split quad" shifts, in which the four beams of a quad are focused to slightly different locations so that they do not exactly overlap.[12]

Figure 1(a) shows the important final optics that control the parameters used here. The beam is pointed away from the center of the target by adjusting the mirror. The center of the beam is shifted a specified distance in the vertical plane, measured perpendicular to its propagation direction, as indicated in Fig. 1(b) for the 50° beams. Defocusing the beam is accomplished by moving the focus lens toward the target. To gain the best uniformity and overlap of the laser beams, the diameter of the beam spot generally corresponds to the diameter of the target shell, although the defocus distance is adjusted in the optimized PD designs to change the relative intensities of the four rings of beams. Slightly different pointing shifts can be applied to the four beams of a quad [Fig. 1(c)].

The sizes of the indirect-drive phase-plate focal spots are determined from clearance issues associated with the laser entrance holes in the hohlraum. The NIF will initially have two types of phase plates: Those for inner beams (rings 1 and 2) and those for outer beams (rings 3 and 4). The phase plates will produce elliptical focal spots with the ellipticity dependent on the angles at which the beams enter the hohlraum. Since the beams in rings 3 and 4 pass more obliquely through the laser entrance holes, their spot sizes are smaller than those for rings 1 and 2.

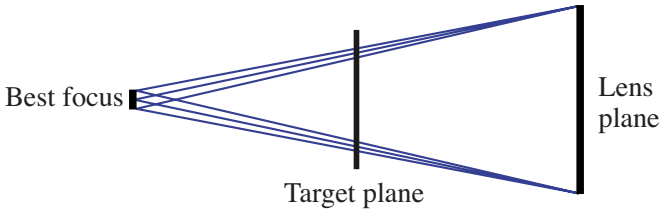

FIG. 2. (Color online) Geometrical-optics model used for calculating out-of-focus target-plane profiles given the best-focus distribution. Rays with a spread of angles are launched from each of a grid of points on the lens plane.

A simple geometrical-optics model is used to calculate the target-plane intensity profile that results from defocusing a laser beam, assuming only that the best-focus distribution is given. Referring to Fig. 2, the lens is subdivided into a large number of elements (typically 400×400) and a number of rays are launched from each element toward the best-focus plane with a randomly chosen direction. The ray is accepted with a probability proportional to the best-focus intensity distribution. Rays continue to be launched from an element until a specified number (typically 10) have been accepted. Each accepted ray has an equal weight and contributes to the out-of-focus intensity distribution at the point where it intercepts the target plane. The model is well suited to beams with a phase plate in the lens plane, when each point on the phase plate can be thought of as imparting an angular spread to the beam that matches the best-focus intensity distribution.

Figures 3(a)–3(d) show predictions for the target-plane intensity contours in best focus and out of best focus, with and without phase plates. The size of the best-focus spot [Fig. 3(a)] is determined by the optical aberrations in the laser; for illustrative purposes, a Gaussian profile of 133 μm full width at half maximum was assumed. Without a phase plate, the spot becomes increasingly square as the beam is moved from best focus [Fig. 3(c)]. The best-focus phase-plate distribution [Fig. 3(b)] is taken from a simple model provided by Munro.[15] The 50% intensity contours are specified as ellipses with $(a,b)=(739,636)$ μm for the inner beams and $(593,343)$ μm for the outer beams. In the model, the intensity elsewhere is given as a function of the distance from this contour, independent of angle. Final PD designs for the NIF will be adjusted when the final values of a and b are selected, and will incorporate an improved model of NIF beams[16] based on simulations and measurements of actual beam near fields. Some noise in the contours is seen due to the finite number of rays (given by the typical parameters quoted above); in practice, far greater modulations will be realized due to speckle, but the target designs discussed here are not expected to be sensitive to speckle and its resulting imprint.

The four beams of each quad, arranged at the output of

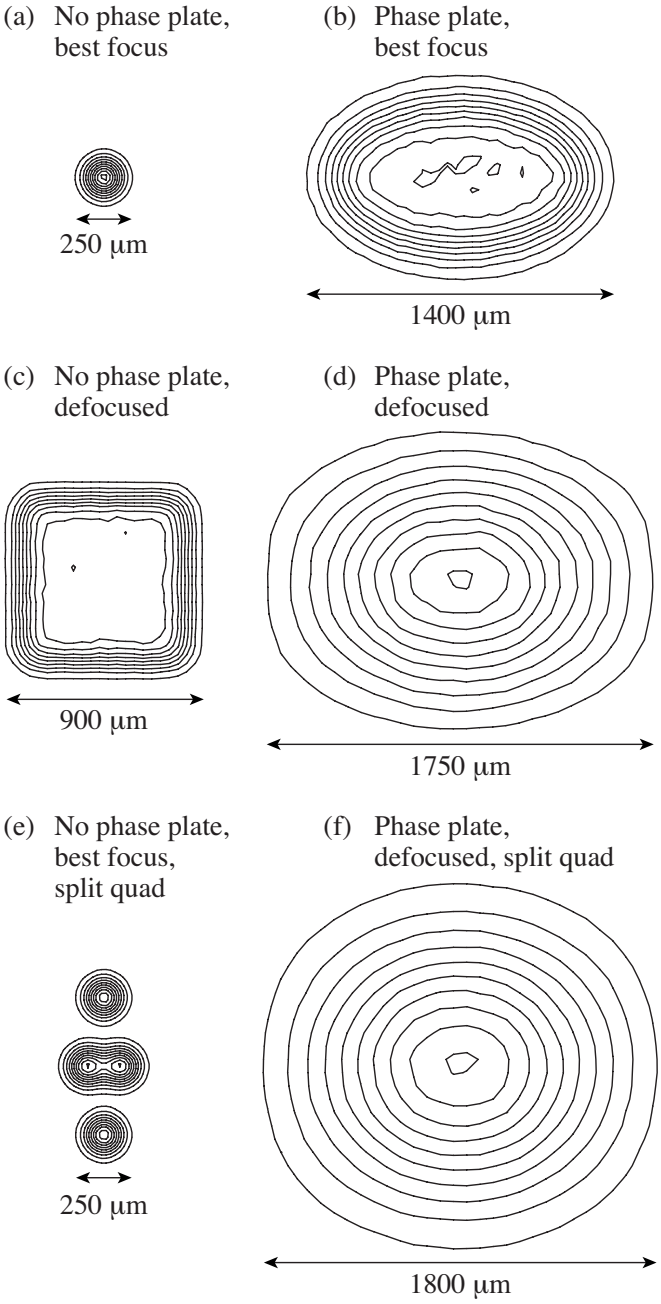

FIG. 3. Target-plane intensity contours for a ring-4 beam. Each contour represents a 10% increase in intensity starting with 10% of peak intensity, except that the innermost contour represents 99%. (a) Best focus, without a phase plate. (b) Best focus, with a phase plate. (c) Defocused 1.3 cm, without a phase plate. (d) Defocused 1.3 cm, with a phase plate. (e) As (a), but with a split quad (two beams shifted ± 75 μm in x, two shifted ± 300 μm in y). (f) The full combination of phase plate, defocus, and split quad as used in the design.

the laser as shown in Fig. 1(c), are usually focused to a single focal spot. However, using split quads, it is possible to alter the shape of the on-target distribution, forming a smoother and wider profile. Figure 3(e) shows a contour plot of a ring-4 beam using split quads at best focus, shifted ± 75 μm and ± 300 μm in the horizontal (x) and vertical (y) directions, respectively. Out of focus and with phase plates, these shifts result in Fig. 3(f), the profile used for one of the optimized designs. By using a combination of split-quad shifting and defocusing, the NIF beams can be enlarged by more than a factor of 2.

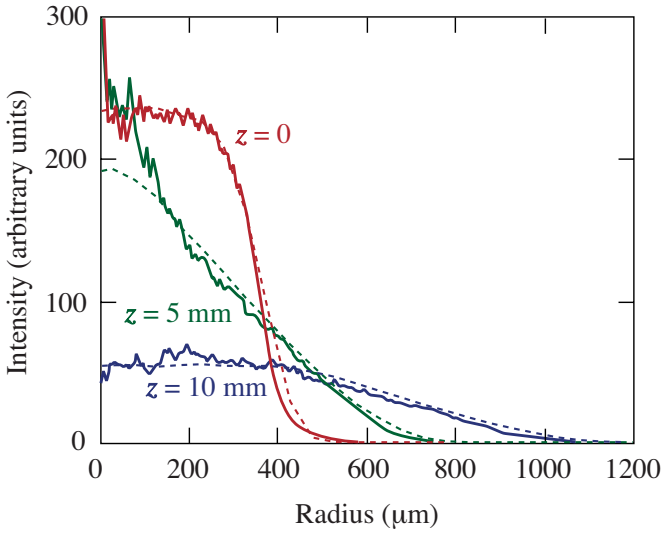

FIG. 4. (Color online) Graphs of intensity vs radius of an OMEGA beam at best focus ($z=0$) and for two defocus distances ($z=5$ mm and 10 mm). The solid lines correspond to experimental data and the dashed lines to simulations.

The geometrical-optics model has been tested by comparison with data obtained from an OMEGA beam.[17] In Fig. 4, azimuthally averaged intensities obtained from equivalent-target-plane images from an "SG4" phase plate (without additional beam smoothing) are compared with the model at best focus and at two defocus distances (5 mm and 10 mm). The intensity profile initially becomes less flat as the distance z from best focus increases to 5 mm. As z increases further, the profile becomes flatter and then approaches the near-field irradiance profile for very large focal shifts. The best focus was fit to a Gaussian of order 7 [intensity $\alpha \exp(-r/r_0)^n$ with $n=7$ and $r_0=380$ μm]. The agreement with the model is very close, except in a small area near the center of the beam for $z=5$ mm, where nonuniformities resulting from phase errors in the near field (not included in the calculation) are not effectively averaged out.

III. OPTIMIZED DESIGN AT 350 kJ

The target design used to optimize the irradiation uniformity at a total laser energy of 350 kJ is a shell of 6 μm of glass (SiO_2) overcoated with 4 μm of plastic (CH), with a radius of 1100 μm (modeled in 2D for simplicity as a 1100 μm shell of the equivalent mass, 8 μm of SiO_2). The shell is filled with 10 atm of deuterium–tritium (DT) gas. The laser pulse used on this target is the Gaussian-shaped pulse shown in Fig. 5(a) with its peak power at 2.5 ns. The motion of the center of mass of the shell, as predicted by SAGE, is shown in Fig. 5(b). Peak compression of the gas inside the target shell occurs around 3.3 ns and the yield predicted by a 1D LILAC calculation (with a simplified, 1D representation of the incident laser beam) is 4.7×10^{15} neutrons. (A variant of this design, with a greater thickness of CH, produced 9×10^{15} neutrons, as discussed in Sec. IV.) Figure 5(b) also shows the time history of a number of den-

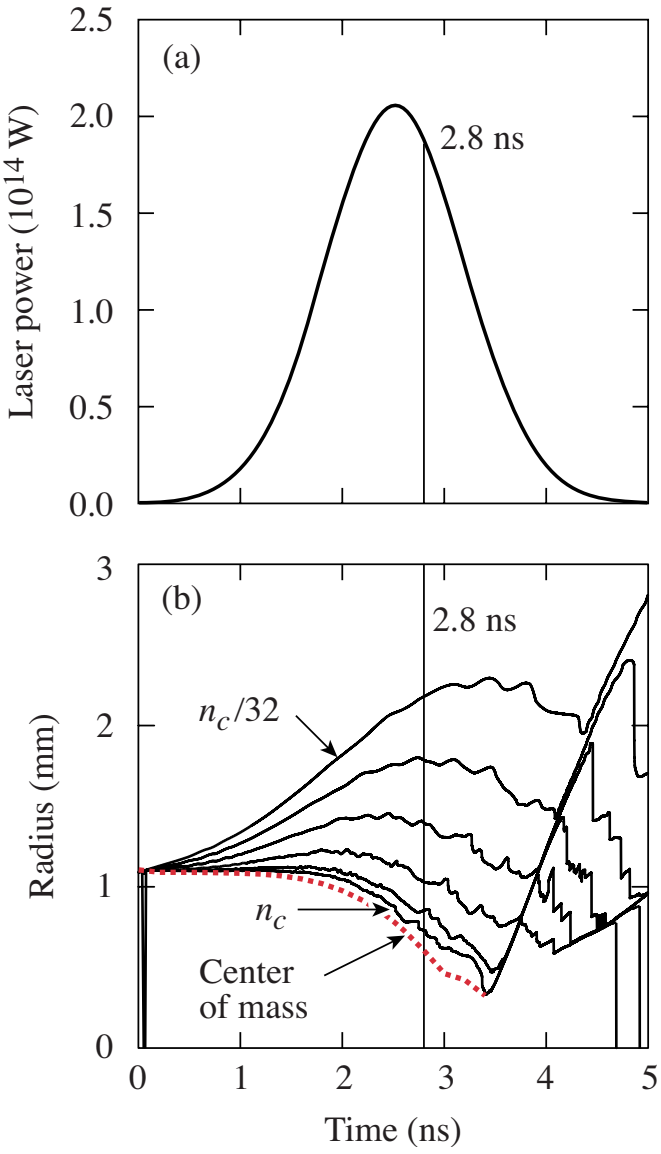

FIG. 5. (Color online) (a) Laser power vs time (a 1.6-ns Gaussian) for a 350-kJ target. (b) Radius vs time of several density contours in the coronal plasma, including critical density (n_c). The center of mass radius of the imploding target shell is shown as a dotted line; its uniformity is typically diagnosed at 2.8 ns for a 350 kJ target.

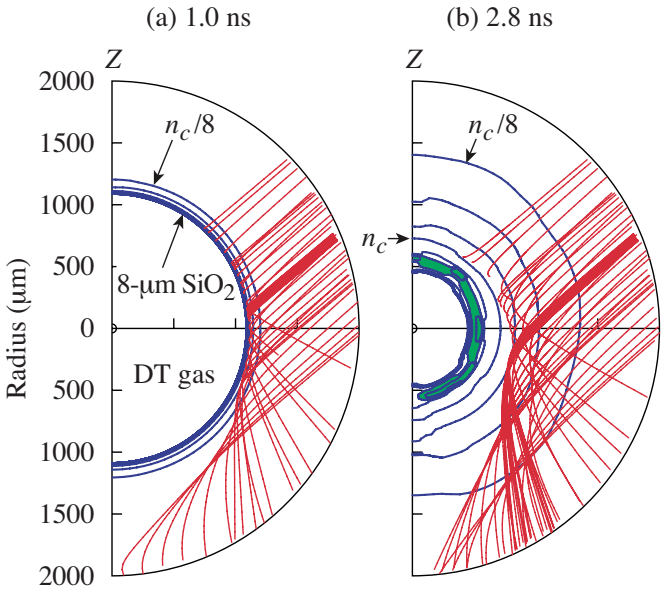

FIG. 6. (Color online) (a) A ray-trace plot at 1.0 ns, near the start of the laser pulse. (b) A ray-trace plot at 2.8 ns, when the shell (density above $4n_c$, green shaded area) has imploded halfway. These plots show representative rays of ring 4 and some density contours.

sity contours, including the critical density (n_c); most of the laser energy is deposited between critical density and the quarter-critical density. A flux limiter[18] f of 0.06 was used in all simulations presented here except where otherwise stated; this value is consistent with the performance of previous PD experiments on OMEGA.[2]

The implosion of the shell and the creation of a coronal plasma are shown in Fig. 6 at an early time (1 ns) and when the shell has imploded halfway (2.8 ns). The figure shows some of the incoming rays from a ring-4 laser beam. The green shaded region in Fig. 6(b) shows the position of the dense portion of the shell. Figure 6(b) shows that the shell has maintained its integrity and uniformity through 2.8 ns. Between 2.8 ns and peak compression, the shell disassembles rapidly as it implodes.

As in previous work[2,3] the uniformity was analyzed on the basis of the center-of-mass radius and velocity as functions of angle θ from the z axis. Typical plots of these quantities at two successive times (2.5 ns and 2.8 ns) are shown in Fig. 7 for an optimized design at 350 kJ. The nonuniformity generally increases with time as small distortions are magnified. At 2.8 ns, the center-of-mass radius is uniform with a root-mean-square (rms) deviation of 6.5 μm (averaged over a solid angle of 4π) and the velocity has a rms deviation (ΔV_{rms}) of 1.7%. Since the target design does not depend on high convergence, this uniformity is considered to be sufficient to ensure an effectively 1D implosion.

The simulation code sometimes produced some numerical noise such as the false peaks at 180° at 2.8 ns in Fig. 7(a) and at 180° at 2.5 ns in Fig. 7(b), but these only led to overestimates of the rms nonuniformity. These false peaks often disappear when the initial conditions are changed very slightly, e.g., by small changes in the zoning or the number of rays used. Much of the residual 1.7% velocity nonuniformity at 2.8 ns in Fig. 7(b) appears to be numerical.

The primary goal of the optimization process was to produce the lowest deviation in the shell center-of-mass radius at a late time into the pulse (2.8 ns for the 350 kJ design), just before shell disassembly. The parameters that were varied were the pointing shift, the defocusing distance, and the split-quad x shift and y shift for each ring of beams. When the edges of the target-plane spatial profiles were steep, it was found to be difficult to obtain equal amounts of drive at angles where the beams overlap. Often, the solution to this was to increase the split-quad y shift slightly on the problem rings. The final set of parameters for the 350 kJ design, based on numerous simulations, is shown in Table I. There are 16 parameters in total, four for each of the four rings. The small defocus distance used for ring 4 provides the extra drive needed at the equator by increasing the intensity of the ring-4 beams relative to the other beams. Split quads are

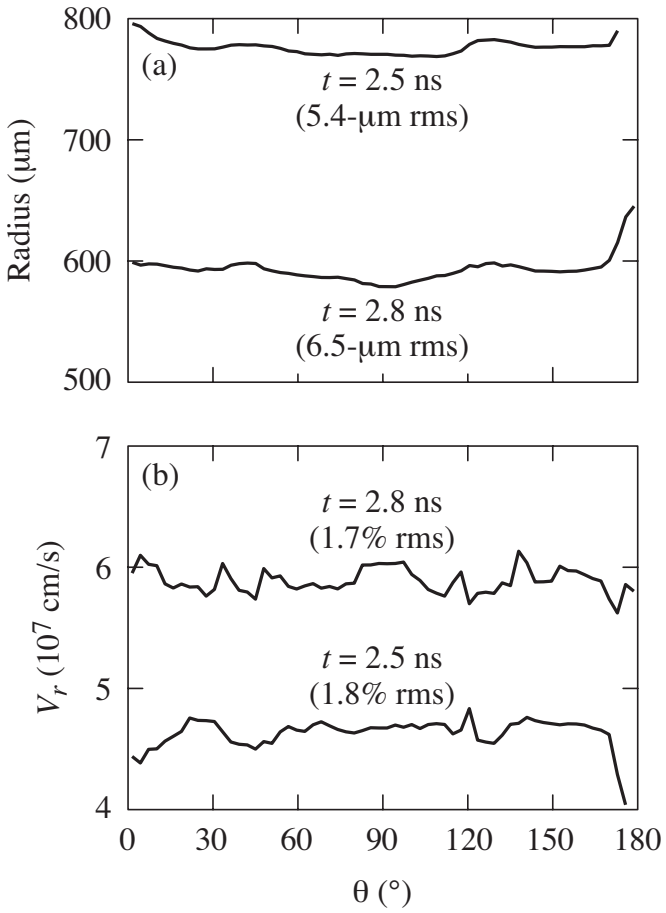

FIG. 7. (a) The center-of-mass radius and (b) the center-of-mass velocity V_r plotted vs angle θ from the z axis for the optimized 350 kJ design, at 2.5 ns and 2.8 ns.

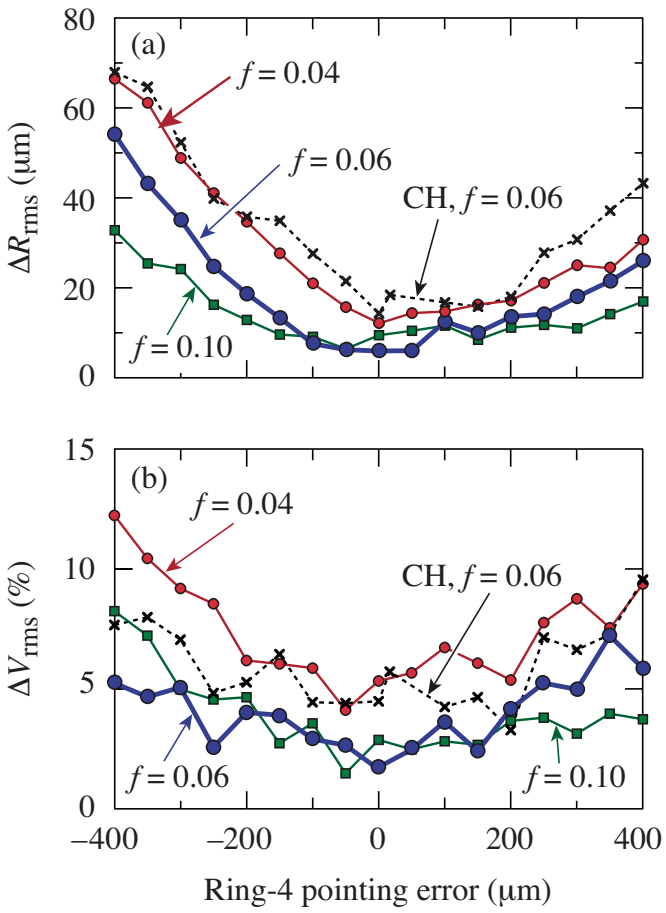

FIG. 8. (Color online) Sensitivity of (a) the rms radius deviation ΔR_{rms} and (b) the rms velocity deviation ΔV_{rms} at 2.8 ns to the pointing errors of ring 4 from the optimum design for SiO_2, for three values of the flux limiter f. The dashed lines show the performance of a CH target using the same design.

used for rings 3 and 4. For ring 4, this smooths out the steeper drop-off of intensity at the edge of the target-plane profile that would otherwise be present from the smaller defocus.

The sensitivity of the design to pointing errors has been explored. In Fig. 8, the deviations from uniformity ΔR_{rms} and ΔV_{rms} are plotted as functions of the ring-4 pointing error. This is done for three values of the flux limiter. Ring 4 is the ring most sensitive to pointing errors because of the tighter focusing. The sensitivity to mispointing of this ring is shown for the worst-case scenario where all of the ring-4 beams are mispointed in the same direction. The values on the horizontal axis are the pointing errors relative to the optimum ring-4 shift (594 μm). For all values of the flux limiter, Fig. 8 shows an insignificant reduction of uniformity for errors in the ± 50 μm range, the NIF pointing specification. Pointings accurate to within 30 μm have been demonstrated,[19] so the pointing control on the NIF is more than adequate for these designs. It is also seen that the optimum pointing depends weakly on the choice of flux limiter, so uncertainties in the details of thermal transport are unlikely to have a significant impact on these designs. The lowest value of f provides the highest nonuniformity.

Figure 8 (dashed lines) also shows the nonuniformity for a CH shell of the same mass as the SiO_2 shell and irradiated with the same pointing and focusing parameters. A larger

TABLE I. Beam-parameter specifications for the optimum design at 350 kJ. Pointing shifts are given for the baseline 8 μm SiO_2 shell and for a 16 μm CH shell.

	Angle	Pointing shift SiO_2	Pointing shift CH	Defocus distance	Phase plate	Split quad x shift	Split quad y shift
Ring 1	23.5°	50 μm	100 μm	2.6 cm	Inner	···	···
Ring 2	30.0°	200 μm	300 μm	2.6 cm	Inner	···	···
Ring 3	44.5°	250 μm	350 μm	2.6 cm	Outer	200 μm	400 μm
Ring 4	50.0°	594 μm	694 μm	1.3 cm	Outer	75 μm	300 μm

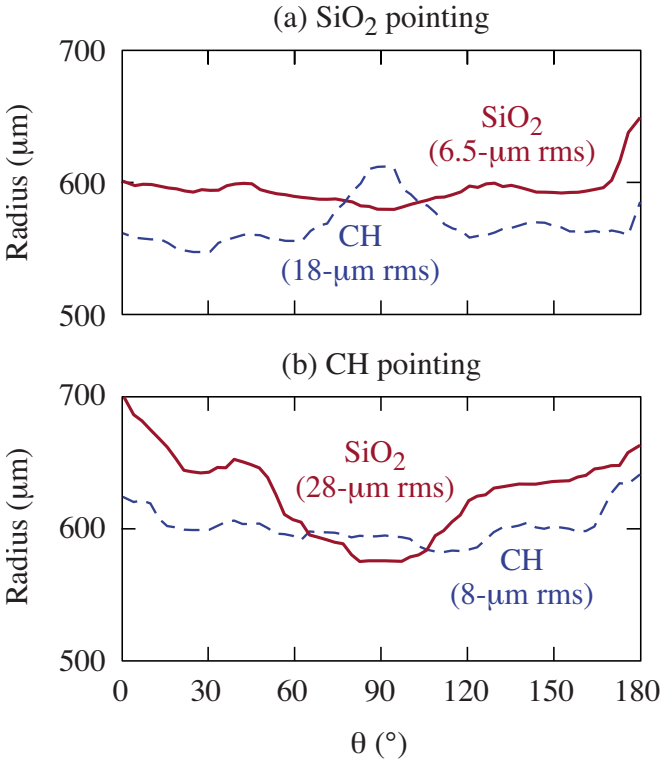

FIG. 9. (Color online) (a) Center-of-mass radius vs angle θ for an 8 μm SiO_2 shell (red, solid) and for a 16 μm CH shell of equivalent mass (blue, dashed), at 2.8 ns, for the baseline pointing optimized for SiO_2. (b) Same as (a) but for pointing shifts optimized for CH.

nonuniformity is found, suggesting that the optimum parameters for CH are different. Since the target will employ an as yet unknown combination of SiO_2 and CH, a final tuning of the pointing parameters for the specific target will be required to optimize the uniformity.

The different results for SiO_2 and CH are illustrated in Fig. 9. In Fig. 9(a), the center-of-mass radius is plotted as a function of angle θ for the baseline SiO_2 target and for the CH target of equivalent mass. Clearly the CH target is underdriven at the equator. This cannot be corrected simply by adjusting the ring-4 pointing. However, by moving all beams toward the equator by 50–100 μm, using the pointing values given in Table I in the column labeled "CH," an irradiation pattern is obtained that provides uniform drive for CH [see Fig. 9(b)]. In this case the SiO_2 is significantly overdriven at the equator.

The reason for the difference between SiO_2 and CH is believed to be related to the different energy deposition profiles along the ray paths. Since the absorption for SiO_2 is slightly higher (by about 10%), relatively more energy is deposited along the initial straight portion of a ray for SiO_2, while relatively more energy in the CH case is deposited on the curved portion of the ray near the turning point, i.e., it is spread over a broader range of angles θ. By the nature of polar drive, this spreading occurs preferentially for rays pointed near the equator, weakening the drive at the equator for the CH case.

While it is anticipated that indirect-drive phase plates will be used for the proposed experiments, it is possible to obtain comparable results without phase plates, using greater split-quad shifts to provide target-plane profiles with comparable shapes.

TABLE II. Specifications of energy-scaled targets with SiO_2 shells.

Energy (kJ)	Outer radius (μm)	Inner radius (μm)	Pulse length (ns)	Peak of pulse (ns)	FWHM (ns)
350	1100	1092	5.0	2.50	1.6
500	1239	1230	5.6	2.82	1.8
1000	1561	1550	7.1	3.55	2.3
1500	1787	1774	8.1	4.06	2.6

IV. OPTIMIZED DESIGNS FROM 350 kJ to 1.5 MJ

Optimized designs have been developed for four different energies (350, 500, 1000, and 1500 kJ). This has enabled best-fit curves to be obtained for each of the focusing and pointing parameters as a function of energy, so that designs at intermediate energies can be readily identified via interpolation.

As the incident laser energy E increases, the linear dimensions of the shell (radius and thickness) and the laser pulse (full width at half maximum) are increased in proportion to $E^{1/3}$. The parameters determined using this relationship are shown in Table II. (It should be cautioned that an amended laser pulse shape should be used for energies above 1 MJ to prevent the peak power, which scales as $E^{2/3}$, from exceeding the NIF operating limit; however, initial experiments to activate neutron diagnostics are not likely to need these energies.) The designs for 500, 1000, and 1500 kJ exhibit similar levels of uniformity to the 350-kJ design. They also show a similar degree of sensitivity to pointing errors and will easily tolerate pointing errors of ± 50 μm.

The design points and best-fit curves for ring-1 and ring-4 pointings are shown in Fig. 10. The equations for all parameters and the corresponding coefficients of determination (R^2 values) are shown in Table III. These curves are all excellent fits to the design points as shown by the R^2 values. It will be noted from Table III that the split-quad shifts rather than the defocus distance are used to increase the spot size as the laser energy is increased. This is done to avoid target-plane intensity profiles with steep edges.

Using these best-fit formulas, several designs were tested at intermediate energies with results shown in Fig. 11. The interpolated designs produced deviations from uniformity ΔR_{rms} (plotted as a percentage of the mean center-of-mass radius) and ΔV_{rms} comparable to those of the optimized designs. The values plotted in each of Figs. 11(a) and 11(b) lie within bands that represent variations in the numerical noise from run to run, alluded to in the discussion of Fig. 7 and also seen in Fig. 8. Similar variations can result from different runs with the same input parameters but slightly different zoning, as illustrated by the two pairs of simulation points at 350 kJ and 500 kJ. The lower bounds of the bands in Fig. 11 thus provide the more reliable prediction of the uniformity that may be expected.

Predictions for the neutron yield in the same range of

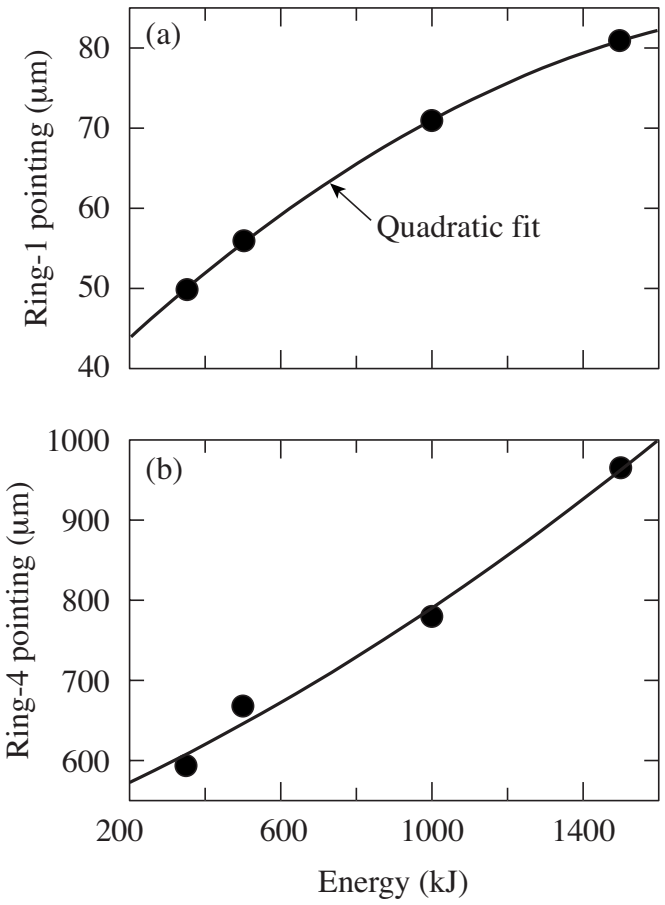

FIG. 10. (a) Ring 1 and (b) ring 4 pointings for the optimized designs at four different energies (solid points). The curves are quadratic best fits.

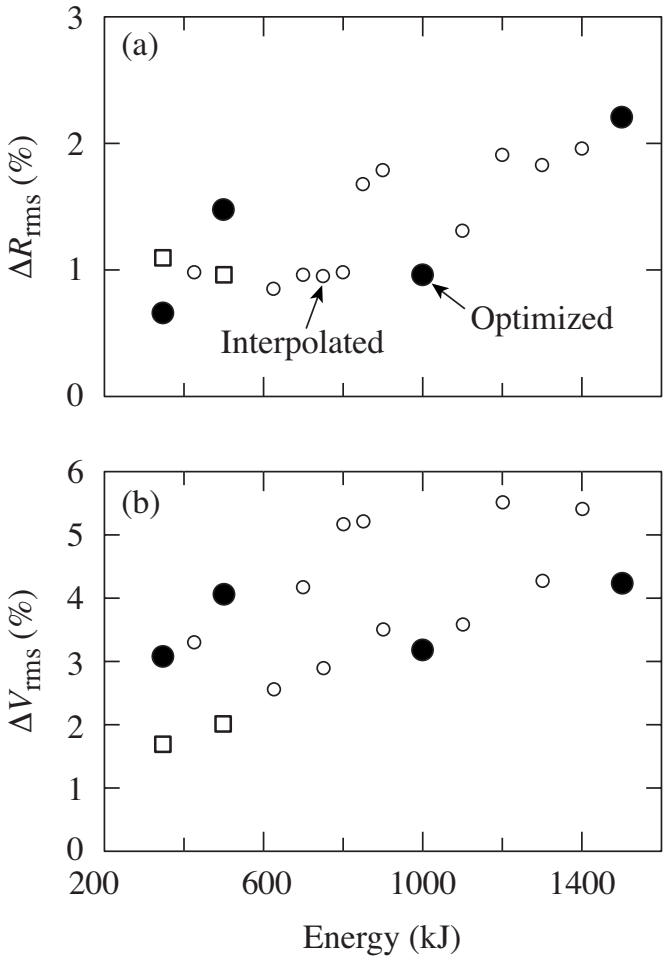

FIG. 11. Predicted rms variations in (a) the center of mass radius and (b) the implosion velocity as a function of laser energy. The solid points were individually optimized while the open circles were obtained using the interpolation formulas of Table III. The open squares are from two runs with slightly different zoning.

laser energies are given in Fig. 12, based on 1D LILAC simulations. The solid square points are for 5-μm-thick SiO_2 targets with a 20 μm CH ablator and the solid circular points are for pure SiO_2 targets of equivalent thickness (15 μm). In each case the target is filled with 10 atm of DT. The target diameters and laser parameters are as given in Table II. Clearly the targets with CH ablators perform better. (This should not be understood to indicate that SiO_2 targets are intrinsically inferior as all-SiO_2 targets have given high yields on OMEGA; it is possible that optimum SiO_2 designs have not yet been identified.) The figure also gives an experimental data point (open triangle) obtained on OMEGA for an SiO_2 target with a CH ablator [10^{14} neutrons at 30 kJ (Ref. 10)] together with the 1D LILAC prediction. The LILAC simu-

TABLE III. Formulas enabling the four pointing and focusing parameters for each ring to be determined for laser energies in the range of 350 kJ–1.5 MJ. The R^2 values for each polynomial fit are also given. [E is the total laser energy (kJ).]

	Ring 1	Ring 2	Ring 3	Ring 4
Pointing shift (μm)	$-1.1\times10^{-5}E^2$ $+0.047E+35$	$-4.96\times10^{-5}E^2+$ $0.275E+106$	$2.37\times10^{-5}E^2+$ $0.0857E+225$	$5.61\times10^{-5}E^2+$ $0.203E+531$
R^2	0.9999	0.9979	0.9974	0.9892
Defocus distance (cm)	2.6	2.6	2.6	1.3
Split quad y shift ΔY (μm)	⋯	$-3.78\times10^{-4}E^2+$ $1.15E-406$	$-8.44\times10^{-5}E^2+$ $0.371E+282$	$-6.44\times10^{-5}E^2+$ $0.28E+212$
R^2	⋯	0.9499	0.9996	0.9995
Split quad x shift ΔX (μm)	⋯	0.5 ΔY	0.5 ΔY	0.251 $\Delta Y-0.739$
R^2	⋯	1.0000	1.0000	0.9997

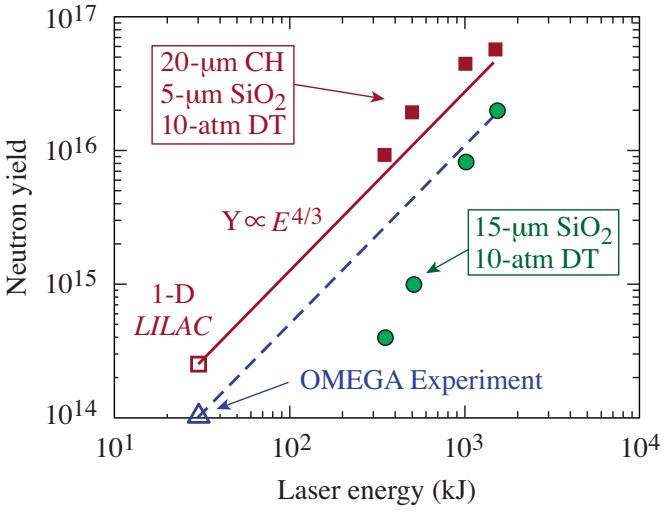

FIG. 12. (Color online) One-dimensional yield calculated by LILAC as a function of laser energy for SiO_2 targets with CH ablators (solid squares, red) and for solid-SiO_2 targets (solid circles, green). The open square and triangle are simulation and experiment, respectively, for an SiO_2 target with a CH ablator irradiated with 30 kJ on the 60-beam OMEGA system. The solid and dashed lines indicate the predicted scaling of yield with energy based on the simple model described in the text.

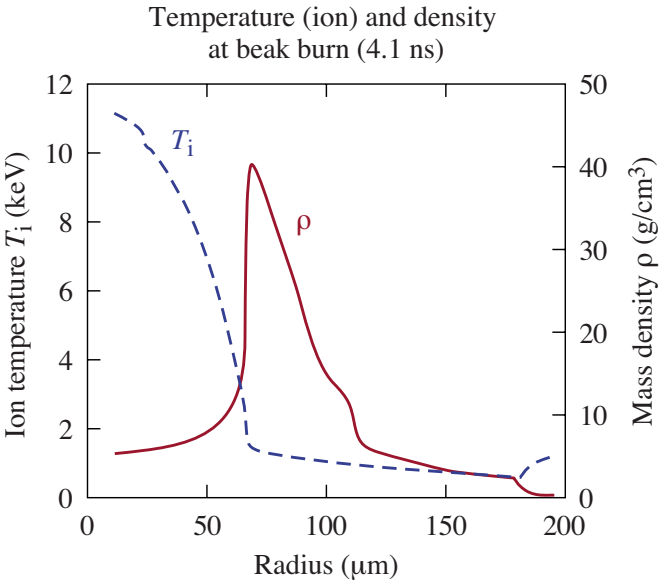

FIG. 13. (Color online) Ion temperature and mass density as functions of radius at the time of peak neutron production (4.1 ns) as predicted by LILAC for a 2.2-mm-diam target with a CH ablator irradiated with 350 kJ of laser energy. The yield was 9.2×10^{15}.

lations for OMEGA and the NIF are consistent with a very simple scaling model in which the yield scales as $E^{4/3}$, where E is the laser energy. In this model it is assumed that the target dimensions and disassembly time scale as $E^{1/3}$ and that the yield scales as the volume times the disassembly time. The solid line indicates this scaling, and the dashed line indicates the same scaling but passes through the OMEGA experimental result. The dashed line gives a yield of just over 10^{16} at 1 MJ. The target designs presented here should not be considered as final as the parameter space of possible designs has not been fully explored.

Profiles of ion temperature and mass density are given in Fig. 13 for the 350 kJ design with the CH ablator at the time of peak neutron production. High temperatures of ~10 keV are attained in a central region of diameter ~100 μm, approximately a factor of 20 smaller than the initial target diameter. The target is not sensitive to hydrodynamic instabilities because the shell disassembles as it implodes and the neutron yield is dominated by the converging shock. Good low-mode uniformity is clearly important, and subsequent work will attempt to quantify this using full 2D simulations.

V. CONCLUSIONS

Thin-shell glass and plastic targets filled with DT have been explored as a means of providing high neutron yields on the NIF for diagnostic development before the implementation of the cryogenic system. Designs providing good irradiation uniformity have been developed at four energy levels using the hydrodynamics code SAGE. Each design involves four parameters per ring of beams: A repointing of the beams toward the equator, a defocus of the beams, and two orthogonal pointing adjustments within each quad to expand the beam overlap on target. Best-fit formulas have been developed for these parameters, making it possible to provide optimal implosion uniformity at energy levels from 350 kJ to 1.5 MJ. These formulas have been found to provide a comparable degree of uniformity throughout the range. Variations of 1%–2% (rms) in center-of-mass radius and 2%–4% (rms) in implosion velocity are anticipated. This uniformity is considered to be more than adequate to obtain the 10^{15} neutrons needed for diagnostic activation. Based on 1D simulations and extrapolation from OMEGA experiments, yields in the range of 10^{15}–10^{16} are expected for laser energies up to 1 MJ. The predicted uniformity is not significantly degraded by anticipated NIF beam-pointing errors. These designs will also enable initial information about polar-drive uniformity to be obtained much sooner than would otherwise be possible.

ACKNOWLEDGMENTS

The authors are grateful for a conversation with Dr. E. Moses, who suggested adjusting the pointings within each quad, Dr. D. Munro and Dr. D. Callahan for providing information on the NIF phase-plate specifications, and Dr. D. D. Meyerhofer and Dr. T. C. Sangster for carefully reading the manuscript and providing many helpful suggestions.

This work was supported by the U.S. Department of Energy Office of Inertial Confinement Fusion under Cooperative Agreement No. DE-FC52-92SF19460, the University of Rochester, and the New York State Energy Research and Development Authority. The support of the DOE does not constitute an endorsement by the DOE of the views expressed in this article.

[1] S. Skupsky, J. A. Marozas, R. S. Craxton, R. Betti, T. J. B. Collins, J. A. Delettrez, V. N. Goncharov, P. W. McKenty, P. B. Radha, T. R. Boehly, J. P. Knauer, F. J. Marshall, D. R. Harding, J. D. Kilkenny, D. D. Meyerhofer, T. C. Sangster, and R. L. McCrory, Phys. Plasmas **11**, 2763 (2004).

[2]R. S. Craxton, F. J. Marshall, M. J. Bonino, R. Epstein, P. W. McKenty, S. Skupsky, J. A. Delettrez, I. V. Igumenshchev, D. W. Jacobs-Perkins, J. P. Knauer, J. A. Marozas, P. B. Radha, and W. Seka, Phys. Plasmas **12**, 056304 (2005).
[3]R. S. Craxton and D. W. Jacobs-Perkins, Phys. Rev. Lett. **94**, 095002 (2005).
[4]J. A. Marozas, F. J. Marshall, R. S. Craxton, I. V. Igumenshchev, S. Skupsky, M. J. Bonino, T. J. B. Collins, R. Epstein, V. Yu. Glebov, D. Jacobs-Perkins, J. P. Knauer, R. L. McCrory, P. W. McKenty, D. D. Meyerhofer, S. G. Noyes, P. B. Radha, T. C. Sangster, W. Seka, and V. A. Smalyuk, Phys. Plasmas **13**, 056311 (2006).
[5]S. Skupsky, R. S. Craxton, F. J. Marshall, R. Betti, T. J. B. Collins, R. Epstein, V. N. Goncharov, I. V. Igumenshchev, J. A. Marozas, P. W. McKenty, P. B. Radha, J. D. Kilkenny, D. D. Meyerhofer, T. C. Sangster, and R. L. McCrory, J. Phys. IV **133**, 233 (2006).
[6]E. M. Campbell and W. J. Hogan, Plasma Phys. Controlled Fusion **41**, B39 (1999).
[7]D. Eimerl, J. Rothenberg, M. Key, S. Weber, C. Verdon, S. Skupsky, J. Soures, and S. Craxton, in *First Annual International Conference on Solid State Lasers for Application to Inertial Confinement Fusion*, edited by M. André and H. T. Powell (SPIE, Bellingham, 1995), Vol. 2633, p. 170.
[8]D. Eimerl, "Configuring the National Ignition Facility for direct-drive experiments," Lawrence Livermore National Laboratory, Livermore, CA, UCRL-ID-120758. See National Technical Information Service Document Report No. DE95017854, 1995 (unpublished). Copies may be ordered from the National Technical Service, Springfield, VA 22161.
[9]V. Yu. Glebov, private communication (2008).
[10]J. M. Soures, R. L. McCrory, C. P. Verdon, A. Babushkin, R. E. Bahr, T. R. Boehly, R. Boni, D. K. Bradley, D. L. Brown, R. S. Craxton, J. A. Delettrez, W. R. Donaldson, R. Epstein, P. A. Jaanimagi, S. D. Jacobs, K. Kearney, R. L. Keck, J. H. Kelly, T. J. Kessler, R. L. Kremens, J. P. Knauer, S. A. Kumpan, S. A. Letzring, D. J. Lonobile, S. J. Loucks, L. D. Lund, F. J. Marshall, P. W. McKenty, D. D. Meyerhofer, S. F. B. Morse, A. Okishev, S. Papernov, G. Pien, W. Seka, R. Short, M. J. Shoup III, M. Skeldon, S. Skupsky, A. W. Schmid, D. J. Smith, S. Swales, M. Wittman, and B. Yaakobi, Phys. Plasmas **3**, 2108 (1996).
[11]T. R. Boehly, D. L. Brown, R. S. Craxton, R. L. Keck, J. P. Knauer, J. H. Kelly, T. J. Kessler, S. A. Kumpan, S. J. Loucks, S. A. Letzring, F. J. Marshall, R. L. McCrory, S. F. B. Morse, W. Seka, J. M. Soures, and C. P. Verdon, Opt. Commun. **133**, 495 (1997).
[12]E. Moses, Lawrence Livermore National Laboratory, private communication (2004).
[13]J. Delettrez, R. Epstein, M. C. Richardson, P. A. Jaanimagi, and B. L. Henke, Phys. Rev. A **36**, 3926 (1987).
[14]R. S. Craxton and R. L. McCrory, J. Appl. Phys. **56**, 108 (1984).
[15]D. Munro, Lawrence Livermore National Laboratory, private communication (2006).
[16]D. Munro, Lawrence Livermore National Laboratory, private communication (2007).
[17]T. J. Kessler, Laboratory for Laser Energetics, private communication (2006).
[18]R. C. Malone, R. L. McCrory, and R. L. Morse, Phys. Rev. Lett. **34**, 721 (1975).
[19]R. A. Zacharias, N. R. Beer, E. S. Bliss, S. C. Burkhart, S. J. Cohen, S. B. Sutton, R. L. Van Atta, S. E. Winters, J. T. Salmon, C. J. Stolz, D. C. Pigg, and T. J. Arnold, in *Optical Engineering at the Lawrence Livermore National Laboratory II: The National Ignition Facility*, edited by M. A. Lane and C. R. Wuest (SPIE, Bellingham, 2004), Vol. 5341, p. 168.